

## Rotation Sensing of a Trapped Nanoparticle Assisted by Magnetic Field Gradient

L.-Y. Wang<sup>✉,1</sup> J.-F. Wei,<sup>1</sup> K.-F. Cui<sup>✉,1</sup> S.-L. Su,<sup>1,\*</sup> M. Feng,<sup>2,3,4</sup> L.-L. Yan<sup>✉,1,†</sup> G. Chen,<sup>1</sup> H.-Z. Guo,<sup>1,‡</sup> and C.-X. Shan<sup>1,§</sup>

<sup>1</sup>Key Laboratory of Materials Physics, Ministry of Education, School of Physics and Microelectronics, Zhengzhou University, Zhengzhou 450001, China

<sup>2</sup>State Key Laboratory of Magnetic Resonance and Atomic and Molecular Physics, Wuhan Institute of Physics and Mathematics, Innovation Academy of Precision Measurement Science and Technology, Chinese Academy of Sciences, Wuhan 430071, China

<sup>3</sup>School of Physics, University of the Chinese Academy of Sciences, Beijing 100049, China

<sup>4</sup>Research Center for Quantum Precision Measurement, Institute of Industry Technology, Guangzhou and Chinese Academy of Sciences, Guangzhou 511458, China



(Received 7 March 2023; revised 21 July 2023; accepted 29 August 2023; published 27 September 2023)

We propose a rotation sensing scheme based on the Sagnac interferometer for a single trapped particle system. In this scheme, the spin and vibrational states of the particle, prepared in a coherent state, are translated into a Schrödinger cat state by applying a strong magnetic field gradient to create the spin-dependent force. By reflecting the phase related to the rotational rate accumulated by the two arms of the interferometer to the spin state, we can obtain the rotational rate of the apparatus by performing spin measurement. The scheme can also be applied to the situation with the vibration state in the thermal state. The sensing sensitivity can reach  $S = 4.47 \times 10^{-7}$  rad/s  $\sqrt{\text{Hz}}$  for a suspended diamond nanoparticle and  $S = 5.65 \times 10^{-6}$  rad/s  $\sqrt{\text{Hz}}$  for a trapped  $^{40}\text{Ca}^+$ . Combining with the experimental parameters, our scheme is applied to realize the gyroscope in a trapped single nanoparticle and atomic ion.

DOI: 10.1103/PhysRevApplied.20.034063

### I. INTRODUCTION

Matter-wave interferometer, due to the high sensitivity against the phase accumulation of the evolution process, has attracted extensive attention in the quantum precision measurement field, such as measuring relativistic effects of electromagnetic interactions [1–3], atomic and molecular properties [4,5], inertial displacements [6–15]. As one of them, the Sagnac interferometer, utilizing the relativistic effect of rotation to accumulate phase difference between two different evolution paths, has been applied for precise rotation sensing [16–22]. The high accuracy and precision of rotation sensing can be used to produce the Sagnac gyroscope in inertial navigation [23–27], geodesy, and geophysics [28,29].

At present, many schemes for gyroscopes with atomic ions have been proposed, and there are also a lot of demonstrations of rotational sensing [10–12,30–33]. Among them, the more widely used method is the construction of

a spin-dependent kick (SDK) using ultrafast pulse generated by mode-locked lasers to entangle the internal and motional states of atomic ions [12,34,35]. The premise of this scheme is that the pulse train is much shorter than the trapping period such that the trap evolution of the ion can be approximately ignored in the process of applying the pulse train. Using the stimulated Raman laser configuration, the laser beam needs to be divided into two beams. The energy-level difference of the chosen two-level system is therefore limited by the laser bandwidth, and two hyperfine energy levels are often chosen for encoding a qubit system [34–36]. On the other hand, two key points are crucial for interferometers, namely apparatus size and sensitivity [11]. To improve the sensitivity, there are two methods, increasing the area enclosed by the interferometer arms or increasing the energy of the interfering particles.

Since the spin-dependent momentum kick generated by the ultrashort pulse of the mode-locked laser [11,12,34,35] is too weeny for the larger masses' nanoparticle to drive the system evolving into a serviceable entanglement state, we propose an alternative rotation sensing scheme, which is not only applicable to the system of trapping atomic ions but also applicable to nanoparticles (such as N-V-center nanocrystals). Besides, it is conducive to the further

\*slsu@zzu.edu.cn

†llyan@zzu.edu.cn

‡hguo@zzu.edu.cn

§cxshan@zzu.edu.cn

improvement of sensitivity. The scheme uses a strong magnetic field gradient (MFG) to drive the spin-dependent position splitting to produce the Schrödinger cat state [37–39], entangling the spin and motion of the nanoparticle. Compared with the laser-induced SDK scheme, it is not constrained by the Lamb-Dicke condition, meanwhile the displacement it induces in the MFG direction is 3 orders of magnitude larger than that produced by SDK. The difference is that an extra spin component will be introduced when the MFG is applied again due to the rotation of the apparatus. To increase the area enclosed by the two arms of the Sagnac interferometer, a displacement is generated by rapidly varying the trapping voltage of the particle in the direction orthogonal to the MFG [40]. Before rapidly varying the trapping voltage to produce an instantaneous displacement, we need to let the particle freely evolve in the trap for a quarter of a period to translate the apparatus rotation rate into the phase shift. In this protocol, the area enclosed by two arms of the interferometer is proportional to the displacement along these two directions and only the coupling driven by the MFG needs to be spin dependent.

The rest of the paper is organized as follows. In Sec. II, we first describe the theoretical model and sensitivity of interferometry. Then, we apply our scheme to the suspended diamond nanoparticle system and  $^{40}\text{Ca}^+$  system to clarify our scheme in Sec. III. Finally, a brief conclusion is given in Sec. IV. The derivation details can be found in the Appendix.

## II. MODEL AND THEORETICAL SCHEME OF THE INTERFEROMETER

A single particle trapped in a Paul trap is used to construct the Sagnac interferometer, where we set the trap frequencies in the  $x$  and  $z$  directions equal ( $\omega_x = \omega_z \equiv \omega$ ), while the  $y$  direction is strongly confined ( $\omega_y \gg \omega$ ) so that the particle can be approximated as two-dimensional motion in the  $z$ - $x$  plane (Fig. 1). The internal energy-level structure of the particle is a universal three-energy system, as shown in the upper right panel of Fig. 1, with two ground states  $|\uparrow\rangle$  and  $|\downarrow\rangle$ , and an excited state  $|e\rangle$ .

Before starting our protocol, we assume that the internal state of the particle is initialized into the spin ground state  $|\downarrow\rangle$  after the optical pumping, meanwhile, the motional state of the particle is in a thermal state  $\rho_{\text{th}}$ , expanded by the coherent state basis vectors as  $\rho_{\text{th}} = \int d^2\alpha P_{\text{th}}(\alpha)|\alpha\rangle\langle\alpha|$  where  $P_{\text{th}}$  is the Glauber  $P$  representation for the thermal state. For simplicity, we start with the initial state as a coherent state  $|\downarrow\rangle|\alpha_z, \alpha_x\rangle$  to elaborate our scheme. Then, the measurement results for the thermal state can be obtained by the thermal average on the brightness of the corresponding coherent state, where the influence of the thermal state, as stated in the following calculations, is reflected in a reduction of the interference contrast.

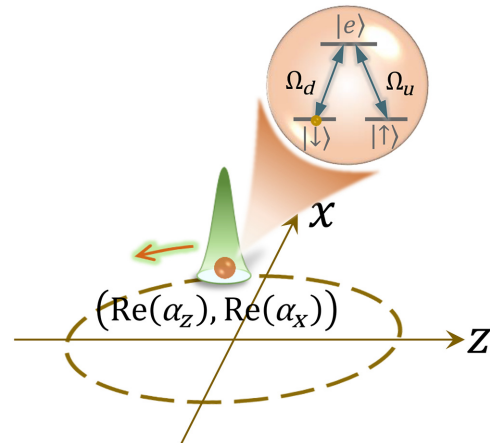


FIG. 1. Schematic diagram of a single-particle motion in the  $z$ - $x$  plane. The internal energy-level structure and the laser configuration of the particle are enlarged in the upper right panel, where  $\Omega_{d,u}$  denote the Rabi frequencies of lasers.

Besides, the coherent state can be prepared by the bang-bang control protocol [40,41], spatially uniform classical driving field, a “moving standing wave,” or pairs of standing waves [42,43].

### A. Interferometer operations for a single particle

To realize the rotational sensing of tiny rotational rate, we assume that the rotational rate  $\Omega_r$  of the apparatus is far smaller than the control parameters of the system, such as the Rabi frequencies of laser ( $\Omega_{d,u}$ ), coupling coefficients ( $\lambda$ ), and vibrational frequency ( $\omega$ ) in the following.

A nine-step interferometric procedure is developed to construct the rotation sensing protocol, where the last four steps are inversions of the first four steps, and between them a long free evolution through step (v) is used to accumulate the Sagnac phase shift. Steps (i) and (ix) are the standard Ramsey interferometric processes. Steps (ii) and (iv) are two ways of generating shifts in phase space, where step (ii) produces a spin-dependent position splitting, while step (iv) allows the two wave-packet trajectories to enclose a confined area simply by a spin-independent displacement generated by adiabatically shifting the position of the trap center in the direction perpendicular to step (ii). The specific steps and operations of protocol to construct the interferometer by a trapped particle are stated as follows:

Step (i): As shown in the upper right panel of Fig. 1, two laser beams are used to prepare the spin state of particle from  $|\downarrow\rangle|\alpha_z, \alpha_x\rangle$  into the superposition

$$|\psi_1\rangle = \frac{1}{\sqrt{2}}(|\downarrow\rangle + |\uparrow\rangle)|\alpha_z, \alpha_x\rangle, \quad (1)$$

through the Hadamard operation [44–50]. Here, we just provide a one-step method, implemented by the nonadiabatic holonomic quantum computation (NHQC) [51], that

two laser beams are simultaneously applied to resonantly drive the transition of internal states through the Hamiltonian  $H_l = \hbar[\Omega_d |\downarrow\rangle\langle e| - \Omega_u |\uparrow\rangle\langle e| + H.c.]/2$  with the Rabi frequency  $\Omega_d/\Omega_u = \tan(\pi/8)$  for the duration  $\tau = 2\pi/\sqrt{\Omega_d^2 + \Omega_u^2}$ . In our protocol, we assume the Rabi frequency  $\Omega_{d,u}$  of lasers is much larger than other characteristic parameters so that we can neglect other interactions during the transition process of internal states.

Step (ii): A gradient magnetic field  $B(z) = B(0) + B'(0)z$  is applied along the  $z$  axis to entangle the electron spin and motion of the particle. The rotation angle of the apparatus during wave-packet splitting induced by the MFG can be ignored due to the tiny rotational rate  $\Omega_r$ . The Zeeman splitting of  $|\downarrow\rangle$  and  $|\uparrow\rangle$  induced by the zeroth-order expansion of  $B(z)$  can be canceled by adding a uniform magnetic field  $-B(0)$  along  $z$ . The Hamiltonian can be written as  $H = \hbar\omega_0\sigma_z/2 + \hbar\omega(a^\dagger a + c^\dagger c) + H_\lambda$  with the coupling terms

$$H_\lambda = \lambda(c + c^\dagger)\sigma_z + \lambda_0(c + c^\dagger), \quad (2)$$

where  $\sigma_z$  is the usual Pauli operator for the states  $|\downarrow\rangle$  and  $|\uparrow\rangle$  with the frequency difference  $\omega_0$ , and  $a$  ( $a^\dagger$ ) and  $c$  ( $c^\dagger$ ) are respectively the annihilation (creation) operators of motional mode along the  $x$  and  $z$  axis with the same trap frequency  $\omega$ . The first term of the above equation denotes the coupling between the spin and motional states induced by the MFG with the coupling strength  $\lambda = (\Delta_\uparrow - \Delta_\downarrow)\mu_B B'(0)z_0/2$ , and the second term is the coupling of the MFG and motion with the coupling strength  $\lambda_0 = (\Delta_\uparrow + \Delta_\downarrow)\mu_B B'(0)z_0/2$  where  $\mu_B$  is the Bohr magneton,  $z_0 = \sqrt{\hbar/2m\omega}$  is the zero-point fluctuation amplitude of particle with mass  $m$ , and the factor  $\Delta_j = m_j g_j$  with  $m_j$  and  $g_j$  corresponding to the magnetic quantum number and Landé g factor of energy level  $j$  ( $j = \uparrow, \downarrow$ ). As shown in Fig. 2(a), the Hamiltonian in Eq. (2) drives the center-of-mass motion of particle wave packet to split to the maximum value  $4\eta$  after half a motional period  $T/2 = \pi/\omega$  where the magnetic Lamb-Dicke parameter  $\eta \equiv \lambda/\hbar\omega$  [37]. The evolution operator can be obtained as (see Appendix A for more details)

$$U_{\text{MFG}}\left(\frac{T}{2}\right) = e^{-i\tau(a^\dagger a + c^\dagger c)} \left( e^{-i\phi_0} D_z [2(\eta_0 + \eta)] |\uparrow\rangle\langle\uparrow| + e^{i\phi_0} D_z [2(\eta_0 - \eta)] |\downarrow\rangle\langle\downarrow| \right), \quad (3)$$

where  $D_z[\cdot]$  denotes the displacement operator acting in the  $z$  direction, and the phase difference  $\phi_0 = \pi(\omega_0/2\omega - 2\eta_0\eta)$  with the magnetic Lamb-Dicke parameter  $\eta \equiv \lambda/\hbar\omega$  and  $\eta_0 \equiv \lambda_0/\hbar\omega$ . After this step, the system state is evolved

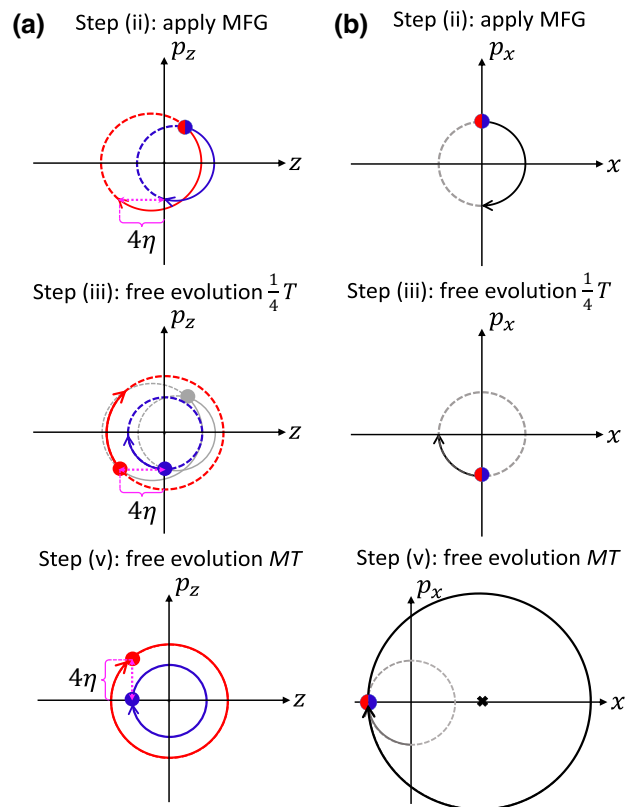


FIG. 2. The evolution of an arbitrary initial coherent state in  $z$  phase space (a) and  $x$  phase space (b), respectively, where the red and blue circles correspond to the  $|\uparrow\rangle$  and  $|\downarrow\rangle$  states, and the black line represents the free evolutionary trajectory of the wave packet without MFG. The red and blue lines represent the evolutionary trajectories of the wave packets with internal states of the particle in  $|\uparrow\rangle$  and  $|\downarrow\rangle$ , respectively.

into the entangled state

$$|\psi_2\rangle = \frac{1}{\sqrt{2}}(e^{-i\phi_0 - i2\eta \text{Im}(\alpha_z)} |\uparrow\rangle |-\alpha_z - 2\eta_0 - 2\eta\rangle + e^{i\phi_0 + i2\eta \text{Im}(\alpha_z)} |\downarrow\rangle |-\alpha_z - 2\eta_0 + 2\eta\rangle) \otimes |-\alpha_x\rangle, \quad (4)$$

with  $\text{Im}(\alpha_z)$  denoting the imaginary part of  $\alpha_z$ .

Step (iii): The particle freely oscillates for a quarter of a vibrational period before the wave packets meet, as shown in step (iii) of Fig. 2 (a), at the end of which the momentum difference between the two wave packets reaches the maximum value  $4\eta$ . The motional state of the system has the form

$$|\mu_{3,\uparrow}\rangle = |i(\alpha_z + 2\eta_0 + 2\eta)\rangle |i\alpha_x\rangle, \quad (5)$$

$$|\mu_{3,\downarrow}\rangle = |i(\alpha_z + 2\eta_0 - 2\eta)\rangle |i\alpha_x\rangle,$$

where  $\mu_{3,j}$  ( $j = \uparrow, \downarrow$ ) represents the motional state of spin  $j$  in step (iii).

Step (iv): The aim of this step is to nonadiabatically ( $t \ll 2\pi/\omega$ ) displace the trap center in the  $x$  direction for a distance  $x_d$ , which can be realized by rapidly moving the center of the trap along the  $x$  axis and the corresponding displacement operator is described as

$$D_x \left[ -\frac{x_d}{2x_0} \right] |i\alpha_x\rangle = \left| i\alpha_x - \frac{x_d}{2x_0} \right\rangle, \quad (6)$$

where  $x_0 = z_0 \equiv \sqrt{\hbar/2m\omega}$  and a global phase is ignored.

Step (v): The particle freely oscillates in the trap for an integer  $M$  period [step (v) in Fig. 2] with interrogation time  $\Delta t = 2\pi M/\omega$  (which is limited by the coherence time  $T_2$ ) to accumulate a Sagnac phase shift. Meanwhile, the rotation of the apparatus will make the direction of the MFG rotate an angle  $\theta = \Omega_r \Delta t$  with the positive direction of  $z$  axis. Here, we choose the nonrotating frame (particle) to describe the rotation effect of the system [11]. Then, the state after step (v) can be described as

$$\begin{aligned} |\psi_5\rangle = \frac{1}{\sqrt{2}} & \left[ e^{-i\phi_{01}-i2\eta\text{Im}(\alpha_z)} |\uparrow\rangle |i(\alpha_z + 2\eta_0 + 2\eta)\rangle \right. \\ & \left. + e^{i\phi_{01}+i2\eta\text{Im}(\alpha_z)} |\downarrow\rangle |i(\alpha_z + 2\eta_0 - 2\eta)\rangle \right] \left| i\alpha_x - \frac{x_d}{2x_0} \right\rangle, \end{aligned} \quad (7)$$

where  $\phi_{01} = \phi_0 + (M + \frac{1}{4}) \omega_0 T$ .

Step (vi): Reverse step (iv) by the reversed nonadiabatically displacement operator, stated as

$$D_x \left[ \frac{x_d}{2x_0} \cos \theta \right] D_z \left[ -\frac{x_d}{2z_0} \sin \theta \right], \quad (8)$$

then, the state of the system is changed into

$$|\psi_6\rangle = \frac{1}{\sqrt{2}} \left[ e^{i\phi_{02}} |\uparrow\rangle |i\alpha_1\rangle + e^{-i\phi_{02}} |\downarrow\rangle |i(\alpha_1 - 4\eta)\rangle \right] |\alpha_2\rangle, \quad (9)$$

where the phase factor  $\phi_{02} = -\phi_{01} - 2\eta\text{Im}(\alpha_z) + 2\eta x_d \sin \theta / 2z_0$ , the displacement along  $z$  and  $x$  axis are  $\alpha_1 = \alpha_z + 2\eta_0 + 2\eta + ix_d \sin \theta / 2z_0$  and  $\alpha_2 = i\alpha_x - x_d(1 - \cos \theta) / 2x_0$ , respectively.

Step (vii): Reverse step (iii) by making the particle freely evolve in the trap for  $3T/4$  to close the free evolutionary trajectory so that we can obtain the state of the system as

$$|\psi_7\rangle = \frac{1}{\sqrt{2}} \left( e^{i\gamma_1} |\uparrow\rangle |-\alpha_1\rangle + e^{-i\gamma_1} |\downarrow\rangle |-\alpha_1 + 4\eta\rangle \right) |\alpha_2\rangle,$$

where  $\gamma_1 = \phi_{02} - \frac{3}{4}\omega_0 T$ .

Step (viii): Reverse step (ii) by applying the MFG again to turn off the interferometer. For convenience in the calculation, here the value of  $\omega_0$  is taken as zero. Then, the evolution operator in the original ion frame is thus obtained as (see Appendix B for details)

$$\begin{aligned} U_{\text{MFG}}^r \left( \frac{T}{2} \right) = e^{-i\pi(a^\dagger a + c^\dagger c)} & \left( e^{i2\pi\eta_{0r}\eta_r} D_z [2(\eta_{0r} + \eta_r) \cos \theta] D_x [2(\eta_{0r} + \eta_r) \sin \theta] |\varphi_+\rangle \langle \varphi_+| \right. \\ & \left. + e^{-i2\pi\eta_{0r}\eta_r} D_z [2(\eta_{0r} - \eta_r) \cos \theta] D_x [2(\eta_{0r} - \eta_r) \sin \theta] |\varphi_-\rangle \langle \varphi_-| \right), \end{aligned} \quad (10)$$

where  $|\varphi_+\rangle = \cos(\theta/2) |\uparrow\rangle + \sin(\theta/2) |\downarrow\rangle$  and  $|\varphi_-\rangle = -\sin(\theta/2) |\uparrow\rangle + \cos(\theta/2) |\downarrow\rangle$  are the eigenstates of the spin operator  $\sigma_{zr} = \sigma_z \cos \theta + \sigma_x \sin \theta$  corresponding to the eigenvalue  $\pm 1$ , and the magnetic Lamb-Dicke parameters of MFG are obtained as  $\eta_r = \lambda_r / \hbar\omega$  and  $\eta_{0r} = \lambda_{0r} / \hbar\omega$  with the coupling strength between spin and motion  $\lambda_r = (\Delta_+ - \Delta_-)\mu_B B'(0)z_0/2$  and coupling strength between the MFG and motion  $\lambda_{0r} = (\Delta_+ + \Delta_-)\mu_B B'(0)z_0/2$ . Here, the factor  $\Delta_\pm = m_\pm g_{e\pm}$  with  $m_\pm$  and  $g_{e\pm}$  denoting the magnetic quantum number and Landé  $g$  factors of the eigenstates  $|\varphi_\pm\rangle$ , respectively. Then, the state is changed into

$$\begin{aligned} |\psi_8\rangle = \frac{1}{\sqrt{2}} & \left[ e^{i(\gamma_1+\gamma_2)} \cos \frac{\theta}{2} |\varphi_+\rangle |\alpha_1 - 2(\eta_{0r} + \eta_r) \cos \theta\rangle | - i\alpha_2 - 2(\eta_{0r} + \eta_r) \sin \theta\rangle \right. \\ & + e^{-i(\gamma_1-\gamma_2)} \sin \frac{\theta}{2} |\varphi_+\rangle |\alpha_1 - 4\eta - 2(\eta_{0r} + \eta_r) \cos \theta\rangle | - i\alpha_2 - 2(\eta_{0r} + \eta_r) \sin \theta\rangle \\ & - e^{i(\gamma_1+\gamma_3)} \sin \frac{\theta}{2} |\varphi_-\rangle |\alpha_1 - 2(\eta_{0r} - \eta_r) \cos \theta\rangle | - i\alpha_2 - 2(\eta_{0r} - \eta_r) \sin \theta\rangle \\ & \left. + e^{-i(\gamma_1-\gamma_3)} \cos \frac{\theta}{2} |\varphi_-\rangle |\alpha_1 - 4\eta - 2(\eta_{0r} - \eta_r) \cos \theta\rangle | - i\alpha_2 - 2(\eta_{0r} - \eta_r) \sin \theta\rangle \right] \end{aligned} \quad (11)$$

with the phase factors

$$\begin{aligned}\gamma_2 &= 2\pi\eta_{0r}\eta_r + 2(\eta_{0r} + \eta_r)\cos\theta \left[ \text{Im}(\alpha_z) + \frac{x_d}{2z_0}\sin\theta \right] + 2(\eta_{0r} + \eta_r)\sin\theta \left[ \text{Im}(\alpha_x) + \frac{x_d}{2x_0}(1 - \cos\theta) \right], \\ \gamma_3 &= -2\pi\eta_{0r}\eta_r + 2(\eta_{0r} - \eta_r)\cos\theta \left[ \text{Im}(\alpha_z) + \frac{x_d}{2z_0}\sin\theta \right] + 2(\eta_{0r} - \eta_r)\sin\theta \left[ \text{Im}(\alpha_x) + \frac{x_d}{2x_0}(1 - \cos\theta) \right].\end{aligned}$$

Step (ix): In order to measure the rotation-induced phase, we apply a  $\pi/2$  pulse under the original basis vector  $\{| \uparrow \rangle, | \downarrow \rangle\}$  with a controllable phase shift  $\varphi - \pi/2$  to the spin state, which leads only to a change in the spin state, i.e.,

$$\begin{aligned}| \uparrow \rangle &\rightarrow \frac{1}{\sqrt{2}}(| \uparrow \rangle + e^{-i\varphi}| \downarrow \rangle), \\ | \downarrow \rangle &\rightarrow \frac{1}{\sqrt{2}}(| \downarrow \rangle - e^{i\varphi}| \uparrow \rangle).\end{aligned}$$

Then,  $|\psi_9\rangle$  can be obtained from  $|\psi_8\rangle$  through the above spin transformation. Measurements on the  $| \uparrow \rangle$  to carry the motion-dependent phase shift to the internal state of the particle, where the probability  $p_\uparrow = \langle \psi_9 | \uparrow \rangle \langle \uparrow | \psi_9 \rangle$  is obtained as

$$\begin{aligned}p_\uparrow &= \frac{1}{2} \left[ 1 - e^{-8(\eta_r^2 + \eta^2) + 16\eta_r\eta\cos\theta} \right. \\ &\quad \times \left. \cos \left( \varphi + A_0 + A(\alpha_z) - \frac{A(\alpha_x)}{\pi z_0^2} \sin\theta \right) \right]. \quad (12)\end{aligned}$$

Considering that  $\theta \ll 1$ , only the zero- and first-order interference terms in amplitude  $\theta$  are kept here, and the first-order terms are found to be completely canceled by the calculation. And the coefficients contained in the exponential and trigonometric functions are not approximated, considering that it contains a gain factor  $\eta_r\eta$  on the one hand, and facilitates the later observation of the interference contrast on the other hand (see Appendix C for more details). In Eq. (12), the constant phase shifts  $A_0 = -4\pi\eta_0\eta - 4\pi\eta_{0r}\eta_r$ ,  $A(\alpha_z) = 8(\eta - \eta_r\cos\theta)\text{Im}(\alpha_z)$  and the rotation-dependent phase shift  $A(\alpha_x) = 8\pi z_0^2\eta_r[\text{Im}(\alpha_x) + x_d/2x_0]$ . The additional area  $A(\alpha_z)$  is caused by the ephemeral rotation effect of the MFG, generally much smaller than  $A(\alpha_x)$ . And  $A(\alpha_x)$  is the classical geometric area of the ellipse enclosed by the nanoparticle trajectories in the  $z$ - $x$  plane where the semiminor axis ( $z$  axis) and semimajor axis ( $x$  axis) of the ellipse are corresponding to  $2z_0 2\eta_r$  and  $(x_d + p_i/m\omega)$  with  $2\eta$ , the displacement of the two wave packets from the center-of-mass position in the  $z$  phase space under the MFG,  $p_i = 2p_0\text{Im}(\alpha_x)$  the initial momentum in  $x$  axis, and  $p_0$  the zero-point fluctuation of momentum. Thus, the Sagnac

phase shift can be obtained as

$$\Phi_S = \frac{A(\alpha_x)}{\pi z_0^2} \sin\theta = 2\pi \frac{2mc^2}{hc^2} [2MA(\alpha_x)] \Omega_r,$$

which shows that the effective area vector enclosed by the two arms of the interferometer is  $\mathbf{A} = 2MA(\alpha_x)$  where the particle encloses the elliptical area twice in each period.

For a thermal state, the probability in  $| \uparrow \rangle$  state can be expressed as  $P_\uparrow = \int d^2\alpha P_{\text{th}}(\alpha)p_\uparrow(\alpha)$  with  $P_{\text{th}}(\alpha) = \exp(-|\alpha|^2/\bar{n})/\pi\bar{n}$  denoting the Glauber-Sudarshan  $P$  representation for the initial state in the coherent state basis where  $\bar{n} = 1/(e^{\hbar\omega/k_B T} - 1)$  is the average phonon of vibration under a temperature  $T$  with  $k_B$  denoting the Boltzmann constant. As mentioned above, for simplicity, we treat the motional state as a coherent state, and here we calculate the brightness  $P_\uparrow(\alpha)$  for the thermal state  $\rho_{\text{th}}$  by taking a thermal average of the brightness  $p_\uparrow$  for the coherent state, which has the form of (see appendix D for more details)

$$\begin{aligned}P_\uparrow &= \frac{1}{2} - \frac{1}{2} e^{-16(\eta_r^2 + \eta^2 - 2\eta_r\eta\cos\theta)(\bar{n} + \frac{1}{2})} \\ &\quad \times \cos \left( \varphi + A_0 - \frac{A(0)}{\pi z_0^2} \sin\theta \right). \quad (13)\end{aligned}$$

Obviously, the effect of the thermal state is only reflected in the reduction of contrast, which is proportional to the average phonon number  $\bar{n}$  of the thermal state.

In the low-temperature limit, the exponential damping is small and the interferometer works well. However, in a high temperature, the contrast of  $P_\uparrow$  will exponentially decay to zero with the increase in temperature, which means the interferometer will lose its capacity to produce effective sensing. Particularly, if the effective Lamb-Dicke parameters in step (ii) and (viii) are the same, the exponential damping caused by the thermal effect can be eliminated due to the quite small rotation rate  $\Omega_r$ , thus, the interferometer will work independently on the finite temperature of the nanoparticle.

Afterward, the possible dissipative processes in the interferometric protocol are analyzed. First, with respect to the trapping loss of ion traps, the current trapping time can reach several hours or even days [45,52–57], and the value is much larger than the time scale of our entire interferometric operation process, so we can neglect the trapping

loss. Secondly, during the whole interferometric operation, only the internal state population modulation and projection measurements of step (i) and step (ix) involve the participation of excited state (auxiliary state)  $|e\rangle$ , and we have assumed above that the laser (microwave) Rabi intensity during the processes are strong, so we ignore the spontaneous decay due to the participation of the excited state during the entire interferometric operation. Furthermore, the main source of decoherence in the protocol is the heating of the motional states of the trapped particles due to noise. For ions, the heating due to background gas collisions is small and the main source of noise is the electrical noise on the surface of the trapped electrode [58–62]. However, for nanoparticle, whose surface area is 6 orders of magnitude larger than that of the atomic ion, the motion heating is mainly due to collisions with the background gas. Considering the short operating times of the other steps, the dissipation process is mainly manifested in the long-term free evolution of step (v), which can be described by the master equation as detailed in Appendix E. Ultimately, we obtain the heating rate of the average phonon number as  $d\langle n \rangle/dt = -\gamma \langle n \rangle + N(\omega)\gamma$ , where  $\langle n \rangle$  is the average phonon number of the system and  $\gamma$  is the damping rate, and  $d\langle n \rangle/dt = N(\omega)\gamma$  as it approaches the vibrational ground state [62]. From Eq. (13), it follows that the effect of an increase in phonon number on the final measurement results is manifested as a decrease in interference contrast [58]. And in Sec. III, we will discuss these for specific systems.

## B. The sensitivity of interferometer

For measurements without using any quantum means, the limit of uncertainty achievable for interferometry is the standard quantum limit approximately  $\sqrt{n}$  ( $n$  is the amount of sources utilized) under a shot-noise correspondence. For a shot-noise-limited interferometer that detects a single interference event within the detectable bandwidth  $\Delta f$  at rate  $\dot{N}$ , the uncertainty of the measured phase will be  $\delta\phi \simeq \sqrt{\Delta f/\dot{N}}$ . Then, the sensitivity of the interferometer, the minimum detectable rotation rate within the detection bandwidth  $\Delta f$ , is defined as [11,63]

$$S = \frac{\delta\phi}{\frac{\partial\Phi_S}{\partial\Omega}\sqrt{\Delta f}} = \frac{1}{\frac{\partial\Phi_S}{\partial\Omega}\sqrt{\dot{N}}}, \quad (14)$$

where the scale factor is given by

$$\frac{\partial\Phi_S}{\partial\Omega} = 2\pi A \frac{2E}{hc^2}. \quad (15)$$

Therefore, when the evolution time has been fixed, the sensitivity of the trapped nanoparticle can be obtained as

$$S = \frac{\hbar\omega}{2(\Delta_\uparrow - \Delta_\downarrow)\mu_B B'(0)[x_d + 2x_0\text{Im}(\alpha_x)]\sqrt{\Delta t}}. \quad (16)$$

If the displacement  $x_0\text{Im}(\alpha_x)$  induced by the coherent state is much smaller than the displacement  $x_d$  of trap center, it is reduced to

$$S_{\text{th}} = \frac{\hbar\omega}{2(\Delta_\uparrow - \Delta_\downarrow)\mu_B B'(0)x_d\sqrt{\Delta t}}, \quad (17)$$

which is independent on the initial motional state of the system.

## III. APPLICATION FOR NANOPARTICLES AND ATOMIC IONS

In the theoretical model, we give a universal interference protocol that is suitable for both nanoparticles and atomic ions. We then apply the protocol to the specific N-V-center nanocrystal system and  $^{40}\text{Ca}^+$  ion system trapped in an ion trap.

### A. Application to the suspended N-V-center nanoparticle

We first apply our interference protocol to the nanodiamond system with a negatively charged N-V center [64–69] trapped in an end-cap Paul trap [Fig. 3(a)]. As shown in Fig. 3(b), the N-V center, as a common luminous defect in diamond lattice, owns a spin-triplet ground state  $|^3A_2, m_s = 0, \pm 1\rangle$  where we encode the two-level system as  $|+1\rangle = |^3A_2, m_s = +1\rangle$ , and  $| -1\rangle = |^3A_2, m_s = -1\rangle$ . Following the theoretical protocol, we set the trapped frequencies  $(\omega_x, \omega_y, \omega_z) = 2\pi \times (10, 100, 10)$  kHz [54,55], in which we approximatively treat the N-V-center system as a two-dimensional plane motion.

First, a 532-nm excitation light of 300 ns is applied to polarize the initial spin of the particle to the ground state

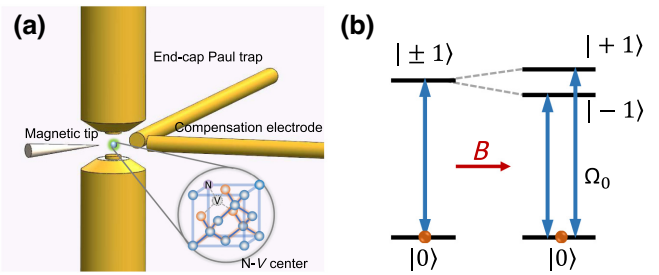


FIG. 3. (a) Diagram of a diamond nanocrystal containing an N-V-center trapped in an end-cap Paul trap, where the direction in which the magnetic tip is located is defined as the  $z$  axis and the axial direction of the end-cap Paul trap is the  $y$  direction. The lattice structure of diamond is enlarged in the lower right-hand panel with the vacancy (transparent), nearest carbon atoms of vacancy (orange), the substitutional nitrogen atom (purple), and carbon atom around the single N-V-center (blue). (b) The ground-state energy-level structure of N-V center where the  $|0\rangle$  energy level has a 2.88-GHz zero-field splitting from the degenerate states  $|\pm 1\rangle$  without magnetic field, and two degenerate can be canceled by the Zeeman effect of magnetic field.

TABLE I. The parameters under applying the MFG for N-V-center system, where the first and third lines show the parameters in steps (ii) and (viii), respectively, and the second and fourth lines represent the values of the corresponding parameters in the first and third lines.

$\Delta_{+1}$	$\Delta_{-1}$	$\lambda$	$\lambda_0$	$\eta$	$\eta_0$
2	-2	$2\mu_B B'(0)z_0$	0	$\lambda/\hbar\omega$	0
$\Delta_+$	$\Delta_-$	$\lambda_r$	$\lambda_{0r}$	$\eta_r$	$\eta_{0r}$
$\sim 2$	$\sim -2$	$\sim \lambda$	0	$\sim \eta$	0

$|0\rangle = |^3A_2, m_s = 0\rangle$ , and the vibrational state of the N-V center is prepared in the coherent state  $|\alpha_z, \alpha_x\rangle$  [40–43]. Afterwards, the magnetic field is necessary to split the two degenerate sublevels to selectively couple  $|0\rangle$  and  $|\pm 1\rangle$  with the corresponding Hamiltonian  $H_{\text{mw}} = (\hbar\Omega_0/2)(|+1\rangle\langle 0| + |-1\rangle\langle 0| + \text{H.c.})$  where the Rabi frequency  $\Omega_0$  is much larger than any other coupling constants in the system so that we can neglect any other interaction when applying the microwave pulses. We assume that these two pulses are split from the same microwave source and frequency modulated by an acousto-optical modulator so that they are considered to have the same initial phase. Then step (i) is finished by applying a  $\pi$  microwave pulse [50]. Alternatively, the particle can also be first pumped to  $|+1\rangle$  or  $|-1\rangle$ , and then use  $|0\rangle$  ( $|^3A_2\rangle$ ) as an intermediate state to resonantly couple  $|0\rangle$  ( $|^3A_2\rangle$ ) with  $|+1\rangle$  and  $|-1\rangle$ , respectively, through two microwave (laser) pulses [48,49,70]. By constructing the Raman process, we generate the Hadamard operation to

$$|\psi_1\rangle = \frac{1}{\sqrt{2}}(|+1\rangle + |-1\rangle)|\alpha_z, \alpha_x\rangle. \quad (18)$$

For the execution of steps (ii) to (viii), we list the necessary parameters in Table I. Since the Landé  $g$  factors of  $|\pm 1\rangle$  for the N-V center are slightly different, for simplicity we approximately set them to be equal and labeled as  $g_e = 2$ . The phases in the theoretical protocol are then taken as

$$\begin{aligned} \gamma_1 &= -2\eta \text{Im}(\alpha_z) + 2\eta \frac{x_d}{2z_0} \sin \theta, \\ \gamma_2 &= 2\eta \cos \theta \left[ \text{Im}(\alpha_z) + \frac{x_d}{2z_0} \sin \theta \right] \\ &\quad + 2\eta \sin \theta \left[ \text{Im}(\alpha_x) + \frac{x_d}{2x_0} (1 - \cos \theta) \right], \\ \gamma_3 &= -\gamma_2. \end{aligned}$$

In step (ix), the measurement process is executed by applying two  $\pi$  microwave pulses with the Hamiltonians  $H_1 = \Omega_0(i e^{i\varphi}|+1\rangle\langle 0| - |-1\rangle\langle 0|)/2 + \text{H.c.}$  and  $H_2 = -\Omega_0(e^{i\varphi}|+1\rangle\langle 0| - i|-1\rangle\langle 0|)/2 + \text{H.c.}$ , where the phase  $\varphi$  of microwave is controlled. The final state is

obtained as

$$\begin{aligned} |\psi_9\rangle &= \frac{1}{2} \left( e^{i\gamma_{\text{tot}}} (|+1\rangle + e^{-i\varphi} |-1\rangle) |\mu_{9,+1}\rangle \right. \\ &\quad \left. - e^{-i\gamma_{\text{tot}}} (e^{i\varphi} |+1\rangle - |-1\rangle) |\mu_{9,-1}\rangle \right), \end{aligned}$$

where the relative phase factor is  $\gamma_{\text{tot}} = \gamma_1 + \gamma_2$ , and  $|\mu_{9,\pm 1}\rangle = |\alpha_z \pm 2\eta(1 - \cos \theta) + i(x_d/2z_0) \sin \theta\rangle |\alpha_x + i(x_d/2x_0)(1 - \cos \theta) \mp 2\eta \sin \theta\rangle$  denotes the corresponding motion state of the internal state  $|\pm 1\rangle$ . Performing the projection measurement on the state  $|+1\rangle$  and keeping to the first order of  $\theta$ , the brightness  $p_{+1} = \langle \psi_9 | +1\rangle \langle +1 | \psi_9 \rangle$  is obtained as

$$p_{+1} = \frac{1}{2} \left[ 1 - e^{-\left(8\eta \sin \frac{\theta}{2}\right)^2 \left(\tilde{n} + \frac{1}{2}\right)} \cos \left( \varphi - \frac{A(\alpha_x)}{\pi z_0^2} \theta \right) \right], \quad (19)$$

where the rotation-dependent phase shift  $A(\alpha_x) = 8\pi z_0^2 \eta [\text{Im}(\alpha_x) + x_d/2x_0]$ . Besides, as shown in Table I, the Lamb-Dicke parameters  $\eta$  and  $\eta_r$  are approximately equal, thus, the interference contrast of the interferometer based on the N-V-center system is not significantly affected by the finite temperature of the diamond.

The sensitivity of the interference scheme, as shown in Eq. (17), is proportional to the square of the coherence time  $\Delta t$ , which can be increased by using the dynamic decoupled sequence to suppress the decoherence of N-V spin [71–73]. Meanwhile, a cryogenic environment can also increase the coherence time, such as, at 77-K cryogenic temperature, the coherent time of the N-V center is observed to be  $T_2 \approx 0.6$  s [74,75]. Thus, it is feasible to take the free evolution time as 10 ms for cryogenic temperature (77 K), which gives free oscillating periods about  $M = 100$  for the vibrational frequency  $\omega_x = \omega_z \equiv \omega = 2\pi \times 10$  kHz. During the interval, the heating rate caused by the collision of gas molecules (mainly hydrogen molecules) under room temperature is  $\Gamma_h = 3p \sqrt{mk_B T_0}/\varrho \omega R = 962$  Hz [76] where  $p = 10^{-7}$  Pa,  $m = 3.34 \times 10^{-27}$  kg,  $T_0 = 300$  K are corresponding to the pressure, mass, and temperature of background gas molecules, and  $\varrho = 3.5$  g/cm<sup>3</sup> [77,78] and  $R = 50$  nm correspond to the density and radius of the nanoparticle. The heating induces an increase in the average phonon number of the particle to  $\Gamma_h \Delta t = 9.62$  for the particle initially cooled to the vibrational ground state, where this heating rate has no prominent effect on the interference contrast of interferometer. Then, the sensing relative to the Earth's rotational rate has full interferometric contrast. By taking the MFG  $B'(0) = 10$  MT/m [79–81] and a trap displacement of  $x_d = 100$   $\mu\text{m}$ , we have the sensitivity  $S = 8.93 \times 10^{-10}$  rad/s  $\sqrt{\text{Hz}}$ . Furthermore, the sensitivity will be higher for the lower-frequency harmonic oscillator or longer coherent time based on the result of Eq. (17).

In addition, under the low trap frequencies and strong MFG conditions, the diamond nanoparticles exhibit strong diamagnetism, which causes a change from the effective vibrational frequency  $\tilde{\omega} = \sqrt{\omega^2 - (\chi/\varrho\mu_0)B'(0)^2}$  with  $\chi$  and  $\varrho$  corresponding to the volume magnetic susceptibility and density of nanoparticle, and  $\mu_0$  denoting the vacuum permeability [76,82–84]. Therefore, for a diamagnetic particle with  $\chi = -2.2 \times 10^{-5}$  [83],  $\varrho = 3.5 \text{ g/cm}^3$  [77,78] and the trapped frequency  $\omega/2\pi = 10 \text{ kHz}$  ( $M = 100$ ), to drown out the frequency change of diamond nanocrystal caused by the diamagnetism where the MFG is set as  $B'(0) = 2 \times 10^4 \text{ T/m}$ , the sensitivity is further modified to  $S = 4.47 \times 10^{-7} \text{ rad/s} \sqrt{\text{Hz}}$ . Compared with the previous studies, which utilized a bulk diamond N-V-center lattice mounted on a rotating stage for sensing, our protocol has a much higher sensitivity. Currently, rotational sensing schemes using a single N-V electron spin [22], the ensemble of electron spin [20], or the ensemble of nuclear spin ( $^{14}\text{N}$  or  $^{13}\text{C}$  nuclear spins) [20,21,85–89] have been proposed, mostly utilizing the rotational rate-dependent geometric phases accumulated on their spin states for sensing, without involving their motional states, and all at room temperature. Among them, in the proposal of Ashok Ajoy *et al.* to use a combination of electron spin and nuclear spin for spin sensing, the theoretical sensitivity can reach  $8.7 \times 10^{-6} \text{ rad/s} \sqrt{\text{Hz}}$  when taking the coherence time of 1 ms for N-V ensemble nuclear spin [21]. In 2021, Soshenko *et al.* presented a proof-of-concept sensing experiment for the combination of ensemble electron spin and nuclear spin with a scale factor of 1.09 [85], while our scheme has a scale factor of approximately  $10^4$  (due to the fact that sensing sensitivity is not specifically given in the text, we use scaling factors for effective comparison). In the same year, Andrey Jarmola *et al.* published experimental work with a sensing sensitivity of  $4.7^\circ \sqrt{s}$  ( $0.08 \text{ rad/s} \sqrt{\text{Hz}}$ ) for a nuclear spin coherence time of 1.95 ms [87]. The sensitivity of the current experimental rotational sensing using the N-V centers are much lower than that of the theoretical scheme. In contrast, our scheme uses mesoscopic diamond nanoparticles to perform rotational sensing based on the Sagnac effect starting from the interference of its motional state, and its sensitivity is higher than the sensitivity in previous theoretical schemes. The experimental implementation of our scheme will facilitate the further improvement of the sensitivity of the N-V-center gyroscope.

## B. Application of interferometer for atomic ions

When the theoretical model is applied to the atomic ions [12,34,35], we take  $^{40}\text{Ca}^+$  ion trapped in the linear Paul trap as an example with the trapping frequency  $(\omega_x, \omega_y, \omega_z) = 2\pi \times (1, 3, 1) \text{ MHz}$  [Fig. 4(a)]. As shown in Fig. 4(b), the qubit is encoded in the ground states  $|4^2S_{1/2}, m_J = -1/2\rangle$  (labeled as  $|g\rangle$ ) and  $|4^2S_{1/2}, m_J = +1/2\rangle$  (labeled as  $|a\rangle$ ) [90], and the lasers are used to pump

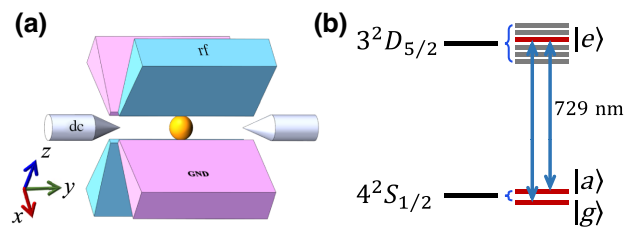


FIG. 4. (a) Schematic diagram of a single  $^{40}\text{Ca}^+$  ion trapped in a linear Paul trap, where blue represents the rf electrode, red represents the GND electrode, and silver represents the cap (dc) electrode. (b) Internal energy-level structure and coding of  $^{40}\text{Ca}^+$ .

the initial state into  $|\psi_1\rangle = \frac{1}{\sqrt{2}}(|g\rangle + |a\rangle)|\alpha_z, \alpha_x\rangle$  through the Hadamard operation [44–47]. The specific parameters of  $^{40}\text{Ca}^+$  ion are substituted into the theoretical model [steps (ii) to (viii)] to obtain Table II.

Then, the phases in this system are taken as

$$\begin{aligned} \gamma_1 &= -2\eta \text{Im}(\alpha_z) + 2\eta \frac{x_d}{2z_0} \sin \theta, \\ \gamma_2 &= 2\pi\eta_0\eta + 2(\eta_0 + \eta) \cos \theta \left( \text{Im}(\alpha_z) + \frac{x_d}{2z_0} \sin \theta \right) \\ &\quad + 2(\eta_0 + \eta) \sin \theta \left( \text{Im}(\alpha_x) + \frac{x_d}{2x_0} (1 - \cos \theta) \right), \\ \gamma_3 &= -2\pi\eta_0\eta + 2(\eta_0 - \eta) \cos \theta \left( \text{Im}(\alpha_z) + \frac{x_d}{2z_0} \sin \theta \right) \\ &\quad + 2(\eta_0 - \eta) \sin \theta \left( \text{Im}(\alpha_x) + \frac{x_d}{2x_0} (1 - \cos \theta) \right). \end{aligned}$$

Ignoring the global phase, the state  $|\psi_9\rangle$  after the execution of step (ix) is

$$|\psi_9\rangle = \frac{1}{2} \left( e^{i\gamma_{\text{tot}}} (|g\rangle + e^{-\varphi} |a\rangle) |\mu_{9,g}\rangle - e^{-i\gamma_{\text{tot}}} (e^{i\varphi} |g\rangle - |a\rangle) |\mu_{9,a}\rangle \right), \quad (20)$$

where the total phase is  $\gamma_{\text{tot}} = -(\pi\omega_0/2\omega) + 4\pi\eta_0\eta - 2\eta \text{Im}(\alpha_z)(1 - \cos \theta) + 2\eta(x_d/2z_0)(1 + \cos \theta) \sin \theta + 2\eta(\text{Im}(\alpha_x) + (x_d/2z_0)(1 - \cos \theta)) \sin \theta$ , and the motion state of ion  $|\mu_{9,g}\rangle = |\alpha_z + 2(\eta_0 + \eta)(1 - \cos \theta) + i(x_d/2z_0) \sin \theta\rangle |\alpha_x + i(x_d/2x_0)(1 - \cos \theta) - 2(\eta_0 + \eta) \sin \theta\rangle$  and  $|\mu_{9,a}\rangle = |\alpha_z + 2(\eta_0 - \eta)(1 - \cos \theta) + i(x_d/2z_0) \sin \theta\rangle$

TABLE II. The relative parameters for  $^{40}\text{Ca}^+$  in the process of applying the MFG.

$\Delta_a$	$\Delta_g$	$\lambda$	$\lambda_0$	$\eta$	$\eta_0$
1	-1	$\mu_B B'(0)z_0$	0	$\lambda/\hbar\omega$	0
$\Delta_+$	$\Delta_-$	$\lambda_r$	$\lambda_{0r}$	$\eta_r$	$\eta_{0r}$
$\sim 1$	$\sim -1$	$\sim \lambda$	0	$\sim \eta$	0

$|\alpha_x + i(x_d/2x_0)(1 - \cos \theta) - 2(\eta_0 - \eta) \sin \theta\rangle$  are corresponding to the internal state  $|g\rangle$  and  $|a\rangle$ . Therefore, the brightness  $p_g = \langle\psi_9|g\rangle\langle g|\psi_9\rangle$  up to the first order of  $\theta$ , is obtained as

$$p_g = \frac{1}{2} \left[ 1 - e^{-\left(8\eta \sin \frac{\theta}{2}\right)^2 \left(\bar{n} + \frac{1}{2}\right)} \right] \times \cos \left( \varphi + A_0 - \frac{A(\alpha_x)}{\pi z_0^2} \sin \theta \right), \quad (21)$$

where the constant phase shifts  $A_0 = \pi\omega_0/\omega - 8\pi\eta_0\eta$ ,  $A(\alpha_z) = 8(\eta - \eta_r)\text{Im}(\alpha_z)$  and the rotation-dependent phase shift  $A(\alpha_x) = 8\pi z_0^2 \eta [\text{Im}(\alpha_x) + x_d/2x_0]$ . Similarly, the interference contrast of interferometer based on  $^{40}\text{Ca}^+$  ion is also not affected by the finite temperature.

For the  $^{40}\text{Ca}^+$  ion, the coherence time can reach 1 s [46], which can give an accessible interrogation time  $\Delta t = 100$  ms with a number of periods about  $M = 10^5$  for the trap frequency of  $\omega/2\pi = 1$  MHz. During this interval, the phonon number of ions cooled to the motional ground state increases by  $\Gamma_h \Delta t = 0.23$  due to the electrode surface noise-induced motional heating [58–62], and here we take the heating rate  $\Gamma_h = 2.3$  Hz [59]. Therefore, it has an affluent capacity to measure the Earth's rotation rate about  $\Omega_r \approx 73 \mu\text{rad/s}$ . The sensitivity is  $S = 5.65 \times 10^{-6} \text{ rad/s} \sqrt{\text{Hz}}$  for the MFG  $B'(0) = 0.1 \text{ MT/m}$  [79–81] and trap displacement of  $x_d = 100 \mu\text{m}$ . The dephasing due to magnetic field fluctuation is suppressed by reducing the MFG and employing dynamic decoupling technique [71,73]. Compared to the scheme proposed by Campbell *et al.* for sensing using  $^{171}\text{Yb}^+$  ions, which has a sensitivity of  $S = 1.4 \times 10^{-6} \text{ rad/s} \sqrt{\text{Hz}}$  when the evolution time is taken as  $\Delta t = 1$  s [11], our scheme has comparable sensitivity but is simpler to operate and more economically advantageous.

When applying the theoretical scheme to a single neutral atom trapped in an optical tweezer, the only difference between its interferometric process and that of a charged particle is that the displacement of the trap center in steps (iv) and (vi) is achieved by changing the electric field to an optical field. There are already some developments in atomic gyroscopes with detection times of 80 ms for laser-cooled atoms and sensitivity up to  $10^{-7} \text{ rad/s} \sqrt{\text{Hz}}$  [91]. The higher sensitivity is due to the huge number of atoms, however, this advantage is not applicable to charged ions. Instead, our scheme focuses on a single-particle system and improves the compactness of the device by increasing the two-wave packet splitting distance, i.e., increasing the scale of the generated Schrödinger cat state, and the number of loops around a fixed area to ensure an large effective interference area.

#### IV. DISCUSSION

The primary requirement of interferometer is creating a strong coupling between the internal and vibrational states of the system used to generate an effective splitting between the particle wave packets, i.e., constructing a Schrödinger cat state [12,34,35,37,38]. To finish this mission, previous atomic ion interferometers required the high-intensity mode-locked pulsed lasers to generate SDKs, together with high costs. The stimulated Raman pulse pair is thus often constructed by splitting the laser beam in two, and the energy difference of the chosen two-level system is limited by the bandwidth of the laser. In contrast, the scheme by using MFG to generate Schrödinger cat states has no special requirements for laser beams, only be used for population transfer during the initial state preparation and readout process, where the wave-packet splitting is generated by MFG-induced coupling, which is more economically advantageous.

On the other hand, the maximum distance of wave-packet splitting generated by both schemes is proportional to the Lamb-Dicke parameter, for nanoparticle systems with small zero-point fluctuation, the tiny optical Lamb-Dicke parameter induced by the laser does not enable effective wave-packet splitting, and therefore the scheme using SDK is not feasible. Instead, the magnetic Lamb-Dicke parameters induced by using the currently achievable MFG of 10 MT/m [79–81] is larger. Moreover, the principle does not limit the particle in the Lamb-Dicke region, thus it can reach a large value, exceeding the optical Lamb-Dicke parameter by about 3 orders of magnitude. Besides, the evolution operator is exactly solved without using the Lamb-Dicke condition where one of the difficulties in the calculation is that the change of the magnetic field direction introduces a component of additional spin directions compared to the laser-induced coupling involving only a single spin direction.

#### V. CONCLUSION

In conclusion, we propose a universal quantum rotational sensing scheme that is not only suitable for single-atom ion systems but especially for nanoparticle systems. For the chosen system, the following four conditions need to be satisfied: (i) a suitable energy-level structure, i.e., the product of the magnetic quantum number  $m_i$  and Landé g factor  $g_i$  of the two selected Zeeman sublevels  $\{\uparrow, \downarrow\}$  is not equal; (ii) vibrational degrees of freedom; (iii) a strong MFG to achieve a strong coupling between the internal and motional states of the system; (iv) a fast adiabatic change in the position of the trap center. Our scheme generates Schrödinger cat states assisted by a strong MFG, is not limited by the Lamb-Dicke condition, simpler in operation, and more economically. Besides, the performance aspect, i.e., the sensitivity, is further improved. The scheme can also be applicable to the thermal-state

situation with a finite temperature. Considering the feasible experimental parameters, the sensitivity can reach  $S = 8.93 \times 10^{-10}$  rad/s  $\sqrt{\text{Hz}}$  for nanoparticle at low environmental temperatures. For the N-V-center system with the low trap frequencies and accessible MFG, the sensitivity can be obtained as  $S = 4.47 \times 10^{-7}$  rad/s  $\sqrt{\text{Hz}}$ . To illustrate the universality of our scheme, we also apply the scheme to the calcium ion system where a sensitivity of about  $S = 5.65 \times 10^{-6}$  rad/s  $\sqrt{\text{Hz}}$  can be obtained. Our scheme will contribute to the experimental exploration related to quantum sensing of a single nanoparticle in solid state.

## ACKNOWLEDGMENTS

This work was supported by Key Research & Development Project of Guangdong Province under Grant No. 2020B0303300001, by the National Key Research & Development Program of China under Grants No. 2017YFA0304503, No. 2021YFA1400204, No. 2021YFA1400900, by National Natural Science Foundation of China under Grants No. 12274376, No. 12204424, No. 12204428, No. 12074232, No. 12125406, No. U21A20434, No. 12074346, No. 12074390, No. 12174347, No. 12147149, No. 91421111, by Natural Science Foundation of Henan Province under Grants No. 202300410481 and No. 212300410085, by K. C. Wong Education Foundation (GJTD-2019-15).

## APPENDIX A: DERIVATION OF UNITARY OPERATOR IN STEP (II)

By making a canonical transformation  $H_e = e^{-iS}He^{iS}$  where  $S = -i(\eta\sigma_z + \eta_0)(c - c^\dagger)$  with the magnetic Lamb-Dicke parameter  $\eta = \lambda/\hbar\omega$  and  $\eta_0 = \lambda_0/\hbar\omega$ , we have

$$H_e = \left( \frac{\hbar\omega_0}{2} - 2\eta_0\lambda \right) \sigma_z + \hbar\omega(a^\dagger a + c^\dagger c). \quad (\text{A1})$$

Then, the corresponding unitary operation  $U = e^{iS}e^{-(i/\hbar)H_{et}}e^{-iS}$  for the Hamiltonian in Eq. (2) is obtained as

$$\begin{aligned} U(t) &= e^{-i\omega(a^\dagger a + c^\dagger c)t - i(\eta\sigma_z + \eta_0)^2 \sin(\omega t) - it(\omega_0/2 - 2\eta_0\lambda)\sigma_z} \\ &\times D_z((\eta\sigma_z + \eta_0)(1 - e^{i\omega t})). \end{aligned} \quad (\text{A2})$$

At the time of half period  $T/2 = \pi/\omega$  with trap frequency  $\omega$ , the above unitary operator can be rewritten as

$$\begin{aligned} U_{\text{MFG}}\left(\frac{T}{2}\right) &= e^{-i\pi(a^\dagger a + c^\dagger c)} \left( e^{-i\phi_0} D_z[2(\eta_0 + \eta)] |\uparrow\rangle\langle\uparrow| \right. \\ &\left. + e^{i\phi_0} D_z[2(\eta_0 - \eta)] |\downarrow\rangle\langle\downarrow| \right), \end{aligned}$$

where  $\phi_0 = \pi[(\omega_0/2\omega) - 2\eta_0\eta]$ . If  $\eta_0 = 0$  and  $\omega_0 = 0$ , ignoring the global phase, it is reduced as

$$U_{\text{MFG}}\left(\frac{T}{2}\right) = D_z[2\eta] |\uparrow\rangle\langle\uparrow| + D_z[-2\eta] |\downarrow\rangle\langle\downarrow|. \quad (\text{A3})$$

Alternatively, we can also utilize Magnus expansion to obtain this result that we rewrite the Hamiltonian in the rotating frame of  $H_0 = \hbar\omega c^\dagger c + \hbar\omega_0\sigma_z/2$  as

$$H_{Iz} = (\sigma_z\lambda + \lambda_0)(ce^{-i\omega t} + c^\dagger e^{i\omega t}). \quad (\text{A4})$$

Therefore, the unitary operator in the rotating frame is  $U_{Iz} = \mathcal{T} \exp[-(i/\hbar) \int H_{Iz}(t) dt]$ , which can be solved with Magnus expansion  $U_{Iz} = \exp[\sum_k \Omega_k(t)]$ . Here, we have

$$\begin{aligned} \Omega_1 &= -\frac{i}{\hbar} \int_0^t H_{Iz}(t_1) dt_1 \\ &= -(\sigma_z\eta + \eta_0)[(e^{i\omega t} - 1)c^\dagger - (e^{-i\omega t} - 1)c], \end{aligned} \quad (\text{A5})$$

and

$$\begin{aligned} \Omega_2 &= \frac{1}{2} \left( -\frac{i}{\hbar} \right)^2 \int_0^t \int_0^{t_1} [H_{Iz}(t_1), H_{Iz}(t_2)] dt_1 dt_2 \\ &= i(\sigma_z\eta + \eta_0)^2 [\omega t - \sin(\omega t)]. \end{aligned} \quad (\text{A6})$$

For  $k \geq 3$ ,  $\Omega_k$  are always equal to zero. Inserting them into  $U_{Iz}$ , we can obtain Eq. (A2).

## APPENDIX B: DERIVATION OF UNITARY OPERATOR IN STEP (VIII)

The Hamiltonian of step (viii) in rotating reference frame (the apparatus frame) can be rewritten as

$$\begin{aligned} H &= \frac{\hbar\omega_0}{2} \sigma_z + \hbar\omega(a_r^\dagger a_r + c_r^\dagger c_r) \\ &+ \mu_B B(\Delta_+|\varphi_+\rangle\langle\varphi_+| + \Delta_-|\varphi_-\rangle\langle\varphi_-|), \end{aligned} \quad (\text{B1})$$

where  $a_r$  and  $b_r$  are obtained by rotating the vibration modes  $a$  and  $b$  under the original reference frame by an angle  $\theta$  around the positive  $y$  axis of the apparatus,  $|\varphi_\pm\rangle$  are the eigenstates of  $\sigma_{zr} = \sigma_z \cos \theta + \sigma_x \sin \theta$  with the corresponding eigenvalues  $\pm 1$ , and  $\Delta_\pm = m_\pm g_{e\pm}$  are the product of magnetic quantum number  $m_\pm$  and Landé  $g$  factors  $g_{e\pm}$  of energy levels  $|\varphi_\pm\rangle$ . For simplicity, we rewrite the above equation as

$$\begin{aligned} H &= \frac{\hbar\omega_0}{2} \sigma_z + \hbar\omega a_r^\dagger a_r + \hbar\omega c_r^\dagger c_r + \lambda_r(c_r + c_r^\dagger)\sigma_{zr} \\ &+ \lambda_{0r}(c_r + c_r^\dagger), \end{aligned} \quad (\text{B2})$$

where  $\lambda_r = (\Delta_+ - \Delta_-)\mu_B B'(0)z_0/2$  is the coupling strength of spin state and motional state induced by the

MFG and  $\lambda_{0r} = (\Delta_+ + \Delta_-)\mu_B B'(0)z_0/2$  is the coupling strength between the MFG and motional state in the rotating frame.

For calculation convenience,  $\omega_0 = 0$  is enabled by choosing two degenerate energy levels to facilitate the exact calculation of the analytic solution of the unitary operator corresponding to the Hamiltonian. Then, by making a canonical transformation  $H'_e = e^{-iS_r} H_e e^{iS_r}$  where  $S_r = -i(\eta_r \sigma_{zr} + \eta_{0r})(c_r - c_r^\dagger)$  with the magnetic Lamb-Dicke parameters  $\eta_r = \lambda_r/\hbar\omega$  and  $\eta_{0r} = \lambda_{0r}/\hbar\omega$ , we can obtain

$$H'_e = -2\eta_{0r}\lambda_r\sigma_{zr} + \hbar\omega a_r^\dagger a_r + \hbar\omega c_r^\dagger c_r, \quad (B3)$$

for which the evolution operator can be easily obtained. Then, the evolution operator  $U'_{\text{MFG}}(t) = e^{iS_r} e^{-(i/\hbar)H'_e t} e^{-iS_r}$  can be calculated as

$$\begin{aligned} U'_{\text{MFG}}(t) &= e^{-i\omega(a^\dagger a + c^\dagger c)t + i2\eta_{0r}\lambda_r\sigma_{zr}t - i|\eta_r\sigma_{zr} + \eta_{0r}|^2 \sin(\omega t)} D_{zr} \\ &\times ((\eta_r\sigma_{zr} + \eta_{0r})(1 - e^{i\omega t})). \end{aligned} \quad (B4)$$

At the time of half period  $T/2 = \pi/\omega$ , we obtain the evolution operator as

$$\begin{aligned} U'_{\text{MFG}}\left(\frac{T}{2}\right) &= e^{-i\pi(a^\dagger a + c^\dagger c)} \left( e^{i2\pi\eta_{0r}\eta_r} D_{zr} [2(\eta_{0r} + \eta_r)] |\varphi_+\rangle\langle\varphi_+| \right. \\ &\left. + e^{-i2\pi\eta_{0r}\eta_r} D_z [2(\eta_{0r} - \eta_r)] |\varphi_-\rangle\langle\varphi_-| \right). \end{aligned}$$

Mapping to the original reference frame, it is stated as

$$\begin{aligned} U'_{\text{MFG}} &= e^{-i\pi(a^\dagger a + c^\dagger c)} \left( e^{i2\pi\eta_{0r}\eta_r} D_z [2(\eta_{0r} + \eta_r) \cos\theta] D_x \right. \\ &\times [2(\eta_{0r} + \eta_r) \sin\theta] |\varphi_+\rangle\langle\varphi_+| + e^{-i2\pi\eta_{0r}\eta_r} D_z [2(\eta_{0r} - \eta_r) \cos\theta] D_x \\ &\left. [2(\eta_{0r} - \eta_r) \sin\theta] |\varphi_-\rangle\langle\varphi_-| \right). \end{aligned}$$

Similarly, this evolution operator can be solved utilizing Magnus expansion, the limitation of which is that Magnus expansion is an approximate solution, where the approximation condition is  $\{\eta_r, \eta_{0r}\} \ll 1$ . This condition

sets a limit to the sensitivity  $S$  of the interferometry that otherwise has no principled limit other than the level of technology.

### APPENDIX C: CALCULATION OF THE FIRST ORDER OF THE BRIGHTNESS $p_\uparrow$ WITH RESPECT TO $\theta$

For convenience, here we denote the four motional states appearing in  $|\psi_8\rangle$  [Eq. (11)] by  $|\mu_a\rangle, |\mu_b\rangle, |\mu_c\rangle, |\mu_d\rangle$ , respectively. Then, rewriting  $|\psi_8\rangle$  under the basis vector  $\{|\uparrow\rangle, |\downarrow\rangle\}$  yields

$$\begin{aligned} |\psi_8\rangle &= \frac{1}{\sqrt{2}} \left[ e^{i(\gamma_1 + \gamma_2)} \left( \cos^2 \frac{\theta}{2} |\uparrow\rangle + \frac{1}{2} \sin \theta |\downarrow\rangle \right) |\mu_a\rangle \right. \\ &+ e^{-i(\gamma_1 - \gamma_2)} \left( \frac{1}{2} \sin \theta |\uparrow\rangle + \sin^2 \frac{\theta}{2} |\downarrow\rangle \right) |\mu_b\rangle \\ &+ \frac{1}{2} e^{i(\gamma_1 + \gamma_3)} \left( \sin^2 \frac{\theta}{2} |\uparrow\rangle - \frac{1}{2} \sin \theta |\downarrow\rangle \right) |\mu_c\rangle \\ &\left. - e^{-i(\gamma_1 - \gamma_3)} \left( \frac{1}{2} \sin \theta |\uparrow\rangle - \cos^2 \frac{\theta}{2} |\downarrow\rangle \right) |\mu_d\rangle \right]. \end{aligned}$$

After applying the  $\pi/2$  pulse from the step (ix) in the main text,  $|\psi_9\rangle$  is easily obtained by substituting the variation of the spin state, i.e.,

$$\begin{aligned} |\uparrow\rangle &\rightarrow \frac{1}{\sqrt{2}}(|\uparrow\rangle + e^{-i\varphi} |\downarrow\rangle), \\ |\downarrow\rangle &\rightarrow \frac{1}{\sqrt{2}}(|\downarrow\rangle - e^{i\varphi} |\uparrow\rangle). \end{aligned}$$

By projecting  $|\psi_9\rangle$  to  $|\uparrow\rangle$ , we obtain

$$p_\uparrow = \frac{1}{2} \left[ 1 - e^{-8(\eta_r^2 + \eta^2) + 16\eta_r\eta \cos\theta} \right. \\ \left. \times \cos \left( \varphi + A_0 + A(\alpha_z) - \frac{A(\alpha_x)}{\pi z_0^2} \sin\theta \right) \right], \quad (C1)$$

where the meaning of each item has been explained under Eq. (12) in the main text. It is calculated that the contribution of each superposition term with a probability amplitude of first order of  $\theta$  in  $|\psi_9\rangle$  is completely canceled by executing the measurement operation of step (ix).

### APPENDIX D: CALCULATION OF THE FIRST ORDER OF THE BRIGHTNESS $p_\uparrow$ WITH RESPECT TO $\theta$

$$\begin{aligned} P_\uparrow &= \int d^2\alpha P_{\text{th}}(\alpha) p_\uparrow(\alpha) = \int d^2\alpha_z P_{\text{th}}(\alpha_z) \int d^2\alpha_x P_{\text{th}}(\alpha_x) \\ &\times \frac{1}{2} \left( 1 - e^{-8(\eta_r^2 + \eta^2) + 16\eta_r\eta \cos\theta} \cos \left( \varphi + A_0 + 8(\eta - \eta_r \cos\theta) \text{Im}(\alpha_z) - 8\eta_r (\text{Im}(\alpha_x) + \frac{x_d}{2x_0}) \sin\theta \right) \right) \end{aligned} \quad (D1)$$

$$\begin{aligned}
&= \int da_z db_z \frac{1}{\pi \bar{n}_z} e^{-(a_z^2 + b_z^2)/\bar{n}_z} \int da_x db_x \frac{1}{\pi \bar{n}_x} e^{-(a_x^2 + b_x^2)/\bar{n}_x} \\
&\quad \times \frac{1}{2} \left( 1 - e^{-8(\eta_r^2 + \eta^2) + 16\eta_r \eta \cos \theta} \cos \left( \varphi + A_0 - 8\eta_r \frac{x_d}{2x_0} \sin \theta + 8(\eta - \eta_r \cos \theta)b_z - 8\eta_r b_x \sin \theta \right) \right) \\
&= \frac{1}{2} - \frac{1}{2} e^{-8(\eta_r^2 + \eta^2) + 16\eta_r \eta \cos \theta} \int da_z db_z \frac{1}{\pi \bar{n}_z} e^{-(a_z^2 + b_z^2)/\bar{n}_z} \int da_x db_x \frac{1}{\pi \bar{n}_x} e^{-(a_x^2 + b_x^2)/\bar{n}_x} \\
&\quad \times \cos \left( \varphi + A_0 - 8\eta_r \frac{x_d}{2x_0} \sin \theta + 8(\eta - \eta_r \cos \theta)b_z - 8\eta_r b_x \sin \theta \right) \\
&= \frac{1}{2} - \frac{1}{2} e^{-16(\eta_r^2 + \eta^2 - 2\eta_r \eta \cos \theta)(\bar{n} + 1/2)} \cos \left( \varphi + A_0 - \frac{A(0)}{\pi z_0^2} \sin \theta \right), \tag{D2}
\end{aligned}$$

where we assume the average number of phonons for both modes of motion is equal, i.e.,  $\bar{n}_z = \bar{n}_x \equiv \bar{n}$ .

## APPENDIX E: THE MOTIONAL HEATING DURING THE FREE FREE EVOLUTION OF STEP (V)

In the long-term free evolution process of step (v), the motion heating caused by noise is described by the master equation

$$\begin{aligned}
\dot{\rho} &= -i[\omega_0 \sigma_z + \omega(a^\dagger a + c^\dagger c), \rho] \\
&\quad + \frac{\Gamma_x}{2} [\bar{N}(\omega) + 1] (2a\rho a^\dagger - a^\dagger a\rho - \rho a^\dagger a) \\
&\quad + \frac{\Gamma_x}{2} \bar{N}(\omega) (2a^\dagger \rho a - a a^\dagger \rho - \rho a a^\dagger) \\
&\quad + \frac{\Gamma_z}{2} [\bar{N}(\omega) + 1] (2c\rho c^\dagger - c^\dagger c\rho - \rho c^\dagger c) \\
&\quad + \frac{\Gamma_z}{2} \bar{N}(\omega) (2c^\dagger \rho c - c c^\dagger \rho - \rho c c^\dagger), \tag{E1}
\end{aligned}$$

where  $\Gamma_{x(z)}$  is the damping rate and  $\bar{N} = (1/e^{\hbar\omega/k_B T} - 1)$  is the thermal occupation of the environment with vibration frequency  $\omega$ , and we define the heating rate  $\Gamma_h = \Gamma_{x(z)} \bar{N}$ . Given the same trapping environment for  $x$  and  $z$  axis, here we assume the damping rate  $\Gamma_x = \Gamma_z \equiv \Gamma$  is feasible. By solving the above equation we obtain the equation of motion for the average thermal occupation number  $\bar{n}_{x,z}$  as

$$\dot{\bar{n}}_{x,z}(t) = -\Gamma \bar{n}_{x,z} + \Gamma_h. \tag{E2}$$

When the system approaches the vibrational ground state, it takes  $\dot{\bar{n}}_{x,z}(t) = \Gamma_h$ .

- [3] Shinya Yanagimachi, Masaki Kajiro, Mamoru Machiya, and Atsuo Morinaga, Direct measurement of the Aharonov-Casher phase and tensor stark polarizability using a calcium atomic polarization interferometer, *Phys. Rev. A* **65**, 042104 (2002).
- [4] Christopher R. Ekstrom, Jörg Schmiedmayer, Michael S. Chapman, Troy D. Hammond, and David E. Pritchard, Measurement of the electric polarizability of sodium with an atom interferometer, *Phys. Rev. A* **51**, 3883 (1995).
- [5] Jörg Schmiedmayer, Michael S. Chapman, Christopher R. Ekstrom, Troy D. Hammond, Stefan Wehinger, and David E. Pritchard, Index of Refraction of Various Gases for Sodium Matter Waves, *Phys. Rev. Lett.* **74**, 1043 (1995).
- [6] Mark Kasevich and Steven Chu, Atomic Interferometry Using Stimulated Raman Transitions, *Phys. Rev. Lett.* **67**, 181 (1991).
- [7] Markus K. Oberthaler, Stefan Bernet, Ernst M. Rasel, Jörg Schmiedmayer, and Anton Zeilinger, Inertial sensing with classical atomic beams, *Phys. Rev. A* **54**, 3165 (1996).
- [8] F. Riehle, Th. Kisters, A. Witte, J. Helmcke, and Ch. J. Bordé, Optical Ramsey Spectroscopy in a Rotating Frame: Sagnac Effect in a Matter-Wave Interferometer, *Phys. Rev. Lett.* **67**, 177 (1991).
- [9] Achim Peters, Keng Yeow Chung, and Steven Chu, Measurement of gravitational acceleration by dropping atoms, *Nature* **400**, 849 (1999).
- [10] T. L. Gustavson, P. Bouyer, and M. A. Kasevich, Precision Rotation Measurements with an Atom Interferometer Gyroscope, *Phys. Rev. Lett.* **78**, 2046 (1997).
- [11] W. C. Campbell and P. Hamilton, Rotation sensing with trapped ions, *J. Phys. B: At. Mol. Opt. Phys.* **50**, 064002 (2017).
- [12] Ami Shinjo, Masato Baba, Koya Higashiyama, Ryoichi Saito, and Takashi Mukaiyama, Three-Dimensional Matter-Wave Interferometry of a Trapped Single Ion, *Phys. Rev. Lett.* **126**, 153604 (2021).
- [13] T. L. Gustavson, A. Landragin, and M. A. Kasevich, Rotation sensing with a dual atom-interferometer Sagnac gyroscope, *Class. Quantum Grav.* **17**, 2385 (2000).
- [14] Ben Stray, *et al.*, Quantum sensing for gravity cartography, *Nature* **602**, 590 (2022).

- [15] Graham P. Greve, Chengyi Luo, Baochen Wu, and James K. Thompson, Entanglement-enhanced matter-wave interferometry in a high-finesse cavity, *Nature* **610**, 472 (2022).
- [16] Brynle Barrett, Rémy Geiger, Indranil Dutta, Matthieu Meunier, Benjamin Canuel, Alexandre Gauguet, Philippe Bouyer, and Arnaud Landragin, The Sagnac effect: 20 years of development in matter-wave interferometry, *C.R. Phys.* **15**, 875 (2014), The Sagnac effect: 100 years later/L'effet Sagnac: 100 ans après.
- [17] Grigorii B. Malykin, The Sagnac effect: Correct and incorrect explanations, *Phys.-Usp.* **43**, 1229 (2000).
- [18] G. A. Vugal'ter and G. B. Malykin, Sagnac effect in ring interferometers on “slow” waves, *Radiophys. Quantum Electron.* **42**, 333 (1999).
- [19] Anatolii A. Logunov and Yu V. Chugreev, Special theory of relativity and the Sagnac effect, *Sov. Phys. Usp.* **31**, 861 (1988).
- [20] M. P. Ledbetter, K. Jensen, R. Fischer, A. Jarmola, and D. Budker, Gyroscopes based on nitrogen-vacancy centers in diamond, *Phys. Rev. A* **86**, 052116 (2012).
- [21] Ashok Ajoy and Paola Cappellaro, Stable three-axis nuclear-spin gyroscope in diamond, *Phys. Rev. A* **86**, 062104 (2012).
- [22] D. Maclaurin, M. W. Doherty, L. C. L. Hollenberg, and A. M. Martin, Measurable Quantum Geometric Phase from a Rotating Single Spin, *Phys. Rev. Lett.* **108**, 240403 (2012).
- [23] G. Mattei, F. Scibona, L. Rosa, M. Lucchesini, A. Esposito, and D. Tonelli, in *2018 DGON Inertial Sensors and Systems (ISS)* (IEEE, Braunschweig, Germany, 2018), p. 1.
- [24] Fernando Vanegas and Felipe Gonzalez, Enabling UAV navigation with sensor and environmental uncertainty in cluttered and GPS-denied environments, *Sensors* **16**, 666 (2016).
- [25] Ahmed Khattab, Yasmine A. Fahmy, and Ahmed Abdel Wahab, High accuracy GPS-free vehicle localization framework via an INS-assisted single RSU, *Int. J. Distrib. Sens. Netw.* **11**, 795036 (2015).
- [26] B. Canuel, F. Leduc, D. Holleville, A. Gauguet, J. Fils, A. Virdis, A. Clairon, N. Dimarcq, Ch. J. Bordé, A. Landragin, and P. Bouyer, Six-Axis Inertial Sensor Using Cold-Atom Interferometry, *Phys. Rev. Lett.* **97**, 010402 (2006).
- [27] Susannah M. Dickerson, Jason M. Hogan, Alex Sugarbaker, David M. S. Johnson, and Mark A. Kasevich, Multiaxis Inertial Sensing with Long-Time Point Source Atom Interferometry, *Phys. Rev. Lett.* **111**, 083001 (2013).
- [28] Heiner Igel, Alain Cochard, Joachim Wassermann, Asher Flaws, Ulrich Schreiber, Alex Velikoseltsev, and Nguyen Pham Dinh, Broad-band observations of earthquake-induced rotational ground motions, *Geophys. J. Int.* **168**, 182 (2007).
- [29] J. K. Stockton, K. Takase, and M. A. Kasevich, Absolute Geodetic Rotation Measurement Using Atom Interferometry, *Phys. Rev. Lett.* **107**, 133001 (2011).
- [30] Alexander D. Cronin, Jörg Schmiedmayer, and David E. Pritchard, Optics and interferometry with atoms and molecules, *Rev. Mod. Phys.* **81**, 1051 (2009).
- [31] Alan Lenef, Troy D. Hammond, Edward T. Smith, Michael S. Chapman, Richard A. Rubenstein, and David E. Pritchard, Rotation Sensing with an Atom Interferometer, *Phys. Rev. Lett.* **78**, 760 (1997).
- [32] D. S. Durfee, Y. K. Shaham, and M. A. Kasevich, Long-Term Stability of an Area-Reversible Atom-Interferometer Sagnac Gyroscope, *Phys. Rev. Lett.* **97**, 240801 (2006).
- [33] A. Gauguet, B. Canuel, T. Lévéque, W. Chaibi, and A. Landragin, Characterization and limits of a cold-atom Sagnac interferometer, *Phys. Rev. A* **80**, 063604 (2009).
- [34] J. Mizrahi, C. Senko, B. Neyenhuis, K. G. Johnson, W. C. Campbell, C. W. S. Conover, and C. Monroe, Ultrafast Spin-Motion Entanglement and Interferometry with a Single Atom, *Phys. Rev. Lett.* **110**, 203001 (2013).
- [35] J. Mizrahi, B. Neyenhuis, K. G. Johnson, W. C. Campbell, C. Senko, D. Hayes, and C. Monroe, Quantum control of qubits and atomic motion using ultrafast laser pulses, *Appl. Phys. B* **114**, 45 (2014).
- [36] W. C. Campbell, J. Mizrahi, Q. Quraishi, C. Senko, D. Hayes, D. Hucul, D. N. Matsukevich, P. Maunz, and C. Monroe, Ultrafast Gates for Single Atomic Qubits, *Phys. Rev. Lett.* **105**, 090502 (2010).
- [37] Zhang-qí Yin, Tongcang Li, Xiang Zhang, and L. M. Duan, Large quantum superpositions of a levitated nanodiamond through spin-optomechanical coupling, *Phys. Rev. A* **88**, 033614 (2013).
- [38] M. Scala, M. S. Kim, G. W. Morley, P. F. Barker, and S. Bose, Matter-Wave Interferometry of a Levitated Thermal Nano-Oscillator Induced and Probed by a Spin, *Phys. Rev. Lett.* **111**, 180403 (2013).
- [39] L. O. Castanos-Cervantes, Quantum Rabi model with dissipation and qubit driving, *Phys. Rev. A* **104**, 033709 (2021).
- [40] J. Alonso, F. M. Leupold, Z. U. Solèr, M. Fadel, M. Marinelli, B. C. Keitch, V. Negnevitsky, and J. P. Home, Generation of large coherent states by bang–bang control of a trapped-ion oscillator, *Nat. Commun.* **7**, 11243 (2016).
- [41] Ryoichi Saito and Takashi Mukaiyama, Generation of a single-ion large oscillator, *Phys. Rev. A* **104**, 053114 (2021).
- [42] D. M. Meekhof, C. Monroe, B. E. King, W. M. Itano, and D. J. Wineland, Generation of Nonclassical Motional States of a Trapped Atom, *Phys. Rev. Lett.* **76**, 1796 (1996).
- [43] Peter A. Ivanov, Nikolay V. Vitanov, and Kilian Singer, High-precision force sensing using a single trapped ion, *Sci. Rep.* **6**, 28078 (2016).
- [44] Ming-Zhong Ai, Sai Li, Zhibo Hou, Ran He, Zhong-Hua Qian, Zheng-Yuan Xue, Jin-Ming Cui, Yun-Feng Huang, Chuan-Feng Li, and Guang-Can Guo, Experimental realization of nonadiabatic holonomic single-qubit quantum gates with optimal control in a trapped ion, *Phys. Rev. Appl.* **14**, 054062 (2020).
- [45] Colin D. Bruzewicz, John Chiaverini, Robert McConnell, and Jeremy M. Sage, Trapped-ion quantum computing: Progress and challenges, *Appl. Phys. Rev.* **6**, 021314 (2019).
- [46] T. Ruster, C. T. Schmiegelow, H. Kaufmann, C. Warschburger, F. Schmidt-Kaler, and U. G. Poschinger, A long-lived Zeeman trapped-ion qubit, *Appl. Phys. B* **122**, 254 (2016).
- [47] H. Häffner, C. F. Roos, and R. Blatt, Quantum computing with trapped ions, *Phys. Rep.* **469**, 155 (2008).
- [48] Silvia Arroyo-Camejo, Andrii Lazariev, Stefan W. Hell, and Gopalakrishnan Balasubramanian, Room temperature

- high-fidelity holonomic single-qubit gate on a solid-state spin, *Nat. Commun.* **5**, 4870 (2014).
- [49] C. Zu, W.-B. Wang, L. He, W.-G. Zhang, C.-Y. Dai, F. Wang, and L.-M. Duan, Experimental realization of universal geometric quantum gates with solid-state spins, *Nature* **514**, 72 (2014).
- [50] Yang Dong, Shao-Chun Zhang, Yu Zheng, Hao-Bin Lin, Long-Kun Shan, Xiang-Dong Chen, Wei Zhu, Guan-Zhong Wang, Guang-Can Guo, and Fang-Wen Sun, Experimental implementation of universal holonomic quantum computation on solid-state spins with optimal control, *Phys. Rev. Appl.* **16**, 024060 (2021).
- [51] Bing-Bing Liu, Fu-Qiang Guo, Lei-Lei Yan, Shou Zhang, Mang Feng, and Shi-Lei Su, Realization of Deutsch–Jozsa algorithm in Rydberg atoms by composite nonadiabatic holonomic quantum computation with strong robustness against systematic errors, *Adv. Quantum Technol.* **4**, 2100093 (2021).
- [52] P. B. Antohi, D. Schuster, G. M. Akselrod, J. Labaziewicz, Y. Ge, Z. Lin, W. S. Bakr, and I. L. Chuang, Cryogenic ion trapping systems with surface-electrode traps, *Rev. Sci. Instrum.* **80**, 013103 (2009).
- [53] Bin Guo, Hua Guan, Qu Liu, Yao Huang, Wan-cheng Qu, Xue-ren Huang, and Ke-lin Gao, Preliminary frequency measurement of the electric quadrupole transition in a single laser-cooled  $^{40}\text{Ca}^+$  ion, *Front. Phys. China* **4**, 144 (2009).
- [54] T. Delord, L. Nicolas, L. Schwab, and G. Hétet, Electron spin resonance from NV centers in diamonds levitating in an ion trap, *New J. Phys.* **19**, 033031 (2017).
- [55] Alexander Kuhlicke, Andreas W. Schell, Joachim Zoll, and Oliver Benson, Nitrogen vacancy center fluorescence from a submicron diamond cluster levitated in a linear quadrupole ion trap, *Appl. Phys. Lett.* **105**, 073101 (2014).
- [56] L. Deslauriers, S. Ölmschenk, D. Stick, W. K. Hensinger, J. Sterk, and C. Monroe, Scaling and Suppression of Anomalous Heating in Ion Traps, *Phys. Rev. Lett.* **97**, 103007 (2006).
- [57] Colin D. Bruzewicz, Robert McConnell, John Chiaverini, and Jeremy M. Sage, Scalable loading of a two-dimensional trapped-ion array, *Nat. Commun.* **7**, 13005 (2016).
- [58] Q. A. Turchette, C. J. Myatt, B. E. King, C. A. Sackett, D. Kielpinski, W. M. Itano, C. Monroe, and D. J. Wineland, Decoherence and decay of motional quantum states of a trapped atom coupled to engineered reservoirs, *Phys. Rev. A* **62**, 053807 (2000).
- [59] L. L. Yan, T. P. Xiong, K. Rehan, F. Zhou, D. F. Liang, L. Chen, J. Q. Zhang, W. L. Yang, Z. H. Ma, and M. Feng, Single-Atom Demonstration of the Quantum Landauer Principle, *Phys. Rev. Lett.* **120**, 210601 (2018).
- [60] I. Pogorelov, T. Feldker, Ch. D. Marciak, L. Postler, G. Jacob, O. Kriegelsteiner, V. Podlesnic, M. Meth, V. Negnevitsky, M. Stadler, B. Höfer, C. Wächter, K. Lakhman-skiy, R. Blatt, P. Schindler, and T. Monz, Compact Ion-Trap Quantum Computing Demonstrator, *PRX Quantum* **2**, 020343 (2021).
- [61] I. Talukdar, D. J. Gorman, N. Daniilidis, P. Schindler, S. Ebadi, H. Kaufmann, T. Zhang, and H. Häffner, Implications of surface noise for the motional coherence of trapped ions, *Phys. Rev. A* **93**, 043415 (2016).
- [62] M. Brownnutt, M. Kumph, P. Rabl, and R. Blatt, Ion-trap measurements of electric-field noise near surfaces, *Rev. Mod. Phys.* **87**, 1419 (2015).
- [63] C. L. Degen, F. Reinhard, and P. Cappellaro, Quantum sensing, *Rev. Mod. Phys.* **89**, 035002 (2017).
- [64] L. Childress, M. V. Gurudev Dutt, J. M. Taylor, A. S. Zibrov, F. Jelezko, J. Wrachtrup, P. R. Hemmer, and M. D. Lukin, Coherent dynamics of coupled electron and nuclear spin qubits in diamond, *Science* **314**, 281 (2006).
- [65] Marcus W. Doherty, Viktor V. Struzhkin, David A. Simpson, Liam P. McGuinness, Yufei Meng, Alastair Stacey, Timothy J. Karle, Russell J. Hemley, Neil B. Manson, Lloyd C. L. Hollenberg, and Steven Prawer, Electronic Properties and Metrology Applications of the Diamond NV<sup>-</sup> Center Under Pressure, *Phys. Rev. Lett.* **112**, 047601 (2014).
- [66] M. W. Doherty, F. Dolde, H. Fedder, F. Jelezko, J. Wrachtrup, N. B. Manson, and L. C. L. Hollenberg, Theory of the ground-state spin of the NV<sup>-</sup> center in diamond, *Phys. Rev. B* **85**, 205203 (2012).
- [67] P. Neumann, R. Kolesov, V. Jacques, J. Beck, J. Tisler, A. Batalov, L. Rogers, N. B. Manson, G. Balasubramanian, F. Jelezko, and J. Wrachtrup, Excited-state spectroscopy of single NV defects in diamond using optically detected magnetic resonance, *New J. Phys.* **11**, 013017 (2009).
- [68] J. R. Maze, A. Gali, E. Togan, Y. Chu, A. Trifonov, E. Kaxiras, and M. D. Lukin, Properties of nitrogen-vacancy centers in diamond: The group theoretic approach, *New J. Phys.* **13**, 025025 (2011).
- [69] Marcus Doherty, Neil Manson, Paul Delaney, Fedor Jelezko, and Lloyd Hollenberg, The nitrogen-vacancy colour centre in diamond, *Phys. Rep.* **528**, 1 (2013).
- [70] Brian B. Zhou, Alexandre Baksic, Hugo Ribeiro, Christopher G. Yale, F. Joseph Heremans, Paul C. Jerger, Adrian Auer, Guido Burkard, Aashish A. Clerk, and David D. Awschalom, Accelerated quantum control using superadiabatic dynamics in a solid-state lambda system, *Nat. Phys.* **13**, 330 (2017).
- [71] I. Cohen, N. Aharon, and A. Retzker, Continuous dynamical decoupling utilizing time-dependent detuning, *Fortsch. Phys.* **65**, 1600071 (2017).
- [72] D. Andrew Golter, Thomas K. Baldwin, and Hailin Wang, Protecting a Solid-State Spin From decoherence Using Dressed Spin States, *Phys. Rev. Lett.* **113**, 237601 (2014).
- [73] Xing-Yan Chen and Zhang-Qi Yin, High-precision gravimeter based on a nano-mechanical resonator hybrid with an electron spin, *Opt. Express* **26**, 31577 (2018).
- [74] M. H. Abobeih, J. Cramer, M. A. Bakker, N. Kalb, M. Markham, D. J. Twitchen, and T. H. Taminiau, One-second coherence for a single electron spin coupled to a multi-qubit nuclear-spin environment, *Nat. Commun.* **9**, 2552 (2018).
- [75] N. Bar-Gill, L. M. Pham, A. Jarmola, D. Budker, and R. L. Walsworth, Solid-state electronic spin coherence time approaching one second, *Nat. Commun.* **4**, 1743 (2013).
- [76] Lv-Yun Wang, Fu-Qiang Guo, S.-L. Su, Chong-Xin Shan, M. Feng, E.-J. Liang, and L.-L. Yan, Rapid ground-state cooling of a solid-state nanoparticle assisted by a magnetic-field gradient, *Phys. Rev. A* **105**, 053124 (2022).

- [77] C. Wan, M. Scala, S. Bose, A. C. Frangeskou, A. T. M. A. Rahman, G. W. Morley, P. F. Barker, and M. S. Kim, Tolerance in the Ramsey interference of a trapped nanodiamond, *Phys. Rev. A* **93**, 043852 (2016).
- [78] A. T. M. A. Rahman, A. C. Frangeskou, M. S. Kim, S. Bose, G. W. Morley, and P. F. Barker, Burning and graphitization of optically levitated nanodiamonds in vacuum, *Sci. Rep.* **6**, 21633 (2016).
- [79] P. Rabl, S. J. Kolkowitz, F. H. L. Koppens, J. G. E. Harris, P. Zoller, and M. D. Lukin, A quantum spin transducer based on nanoelectromechanical resonator arrays, *Nat. Phys.* **6**, 602 (2010).
- [80] P. Rabl, P. Cappellaro, M. V. Gurudev Dutt, L. Jiang, J. R. Maze, and M. D. Lukin, Strong magnetic coupling between an electronic spin qubit and a mechanical resonator, *Phys. Rev. B* **79**, 041302 (2009).
- [81] ZhangQi Yin, Nan Zhao, and TongCang Li, Hybrid optomechanical systems with nitrogen-vacancy centers, *Sci. China Phys. Mech. Astron.* **58**, 1 (2015).
- [82] Jen-Feng Hsu, Peng Ji, Charles W. Lewandowski, and Brian D'Urso, Cooling the motion of diamond nanocrystals in a magneto-gravitational trap in high vacuum, *Sci. Rep.* **6**, 30125 (2016).
- [83] Julen S. Pedernales, Gavin W. Morley, and Martin B. Plenio, Motional Dynamical Decoupling for Interferometry with Macroscopic Particles, *Phys. Rev. Lett.* **125**, 023602 (2020).
- [84] M. C. O'Brien, S. Dunn, J. E. Downes, and J. Twamley, Magneto-mechanical trapping of micro-diamonds at low pressures, *Appl. Phys. Lett.* **114**, 053103 (2019).
- [85] Vladimir V. Soshenko, Stepan V. Bolshedvorskii, Olga Rubinas, Vadim N. Sorokin, Andrey N. Smolyaninov, Vadim V. Vorobyov, and Alexey V. Akimov, Nuclear Spin Gyroscope Based on the Nitrogen Vacancy Center in Diamond, *Phys. Rev. Lett.* **126**, 197702 (2021).
- [86] J.-C. Jaskula, K. Saha, A. Ajoy, D. J. Twitchen, M. Markham, and P. Cappellaro, Cross-sensor feedback stabilization of an emulated quantum spin gyroscope, *Phys. Rev. Appl.* **11**, 054010 (2019).
- [87] Andrey Jarmola, Sean Lourette, Victor M. Acosta, A. Glen Birdwell, Peter Blümler, Dmitry Budker, Tony Ivanov, and Vladimir S. Malinovsky, Demonstration of diamond nuclear spin gyroscope, *Sci. Adv.* **7**, eabl3840 (2021).
- [88] Xuerui Song, Liujun Wang, Fupan Feng, Liren Lou, Wenting Diao, and Chongdi Duan, Nanoscale quantum gyroscope using a single  $^{13}\text{C}$  nuclear spin coupled with a nearby NV center in diamond, *J. Appl. Phys.* **123**, 114301 (2018).
- [89] Alexander A. Wood, Emmanuel Lilette, Yaakov Y. Fein, Nikolas Tomek, Liam P. McGuinness, Lloyd C. L. Hollenberg, Robert E. Scholten, and Andy M. Martin, Quantum measurement of a rapidly rotating spin qubit in diamond, *Sci. Adv.* **4**, eaar7691 (2018).
- [90] Lei-Lei Yan, Lv-Yun Wang, Shi-Lei Su, Fei Zhou, and Mang Feng, Verification of information thermodynamics in a trapped ion system, *Entropy* **24**, 813 (2022).
- [91] Remi Geiger, Arnaud Landragin, Sebastien Merlet, and Franck Pereira Dos Santos, High-accuracy inertial measurements with cold-atom sensors, *AVS Quantum Sci.* **2**, 024702 (2020).